ChemPhysChem

Chemistry Europe
European Chemical Societies Publishing
ChemPhysChem

RESEARCH ARTICLE

Interplay of Solvation Dynamics and Ion Transport in Concentrated LiFSA–Sulfone Electrolytes

Yati | Anirban Mondal

Department of Chemistry, Indian Institute of Technology Gandhinagar, Gandhinagar, Gujarat, India

Correspondence: Anirban Mondal (amondal@iitgn.ac.in)

Received: 14 November 2025 | **Revised:** 13 March 2026 | **Accepted:** 13 March 2026

Keywords: ligand exchange dynamics | lithium-ion transport | metadynamics simulations | solvation structure | sulfone electrolytes

ABSTRACT

Understanding how solvation dynamics govern lithium-ion transport is central to designing high-performance electrolytes. In this work, we combine molecular dynamics (MD) and metadynamics simulations with machine-learned force-field optimization to unravel the interplay between solvation structure, ligand-exchange kinetics, and macroscopic transport in concentrated lithium bis(fluorosulfonyl) amide (LiFSA)–sulfone electrolytes. The results reveal two distinct transport regimes: a solvent-dominated, highly ordered solvation environment in cyclic symmetric sulfolane (SL) that supports long-lived coordination and vehicular-like diffusion with intermittent hopping; and a dynamically flexible, hopping-dominated regime in acyclic and asymmetric solvents ethyl methyl sulfone (EMS), dimethyl sulfone (DMS), 3-methyl sulfolane (MSL) characterized by rapid ligand exchange and fluctuating coordination. Metadynamics free-energy surfaces (FES) confirm that SL stabilizes a deep, solvent-rich solvation basin, while EMS and MSL exhibit broader basins reflecting facile reorganization. The computed residence lengths and exchange rates quantitatively connect these microscopic dynamics to macroscopic trends in viscosity and conductivity, highlighting a tradeoff between solvation stability and dynamic mobility. Together, these insights establish a unified mechanistic framework that links solvation energetics and ion transport, providing molecular-level design principles for optimizing conductivity and stability in next-generation lithium electrolytes.

1 | Introduction

Lithium-ion batteries (LIBs) are the cornerstone of modern energy storage technologies, powering everything from portable electronics to electric vehicles and grid-scale systems [1–5]. However, the safety and performance of conventional carbonate-based electrolytes remain constrained by issues, such as thermal instability, flammability, and limited electrochemical windows [3, 6, 7]. To address these challenges, high-concentration electrolytes (HCEs) and sulfone-based solvents have emerged as promising alternatives due to their high oxidative stability, low volatility, and strong lithium-ion solvation ability [8–11]. Recent experimental and computational studies have demonstrated that sulfone solvents can significantly enhance lithium-ion transference numbers, suppress parasitic reactions, and improve the overall thermal and electrochemical stability of electrolytes [11–15].

Unlike carbonate solvents, sulfones exhibit a markedly different solvation chemistry when paired with salts, such as lithium bis(-fluorosulfonyl)amide (LiFSA) [11, 16–20]. Their highly polar S═O groups [21] and rigid molecular backbones lead to the formation of clustered solvation environments and anion–solvent networks, which in turn give rise to nontrivial ion-transport behavior. In the concentrated regime, lithium conduction has been proposed to occur via a hopping mechanism—mediated by transient rearrangements of coordinated anion–solvent clusters—rather than by classical vehicular diffusion [14, 22–27]. The nature of this hopping process is sensitive to subtle variations in solvent structure, including structure (cycle versus linear), symmetry, and alkyl substitution, which modulate the strength and lifetime of Li—O coordination.

Previous studies have employed various solvent compositions to investigate the conduction mechanism of lithium cations in

different salts, including $LiBF_4$, $LiClO_4$, LiTFSI, and LiFSI. Dokko et al. suggested a hopping mechanism for $LiBF_4$ and $LiClO_4$ salts with a sulfone additive at a 1:3 or lower composition; however, their work did not explicitly consider the influence of solvent molecular structure on the lithium conduction mechanism [14]. Mukherji et al. [12] analyzed the van Hove self and distinct parts to understand the dynamics of lithium ions in a LiFSA–sulfone 1:1 mixture, while Crabb et al. [28] investigated LiTFSI–sulfone systems at dilute compositions (salt-to-solvent atomic ratio of 120:2000), focusing primarily on ion-pair dynamics. However, none of these studies systematically addressed the structural selectivity of solvents or the effects of molecular geometry in the highly concentrated regime. Ikeda et al. [29] further explored LiTFSA–sulfone mixtures across a range of concentrations, emphasizing the evolution of coordination networks around Li^+. However, they did not explicitly consider the competitive coordination between anions and solvent molecules, which ultimately defines the lithium solvation shell.

These prior studies collectively highlight the complexity of ion conduction in sulfone-based electrolytes but leave critical gaps in understanding how molecular symmetry and solvent geometry modulate the balance between Li^+–anion and Li^+–solvent interactions. Moreover, many earlier simulations [13, 30, 31] employed empirical force fields (e.g., OPLS [32, 33]) that inadequately capture the subtle polarization and charge–transfer effects governing ion coordination and hopping dynamics. Our group previously addressed this limitation by developing a machine learning-based active learning framework using a genetic algorithm (GA) and Gaussian process regression (GPR) to derive transferable and physically motivated force fields for LiFSA and a range of sulfone solvents [16, 34]. These force fields have been validated against experimental data on density, surface tension, viscosity, and ionic conductivity and reproduce quantum-mechanical accuracy in solvation structures and dynamic behavior at a fraction of the computational cost.

In the present work, we employ GA-GPR-derived force fields to investigate the microscopic structure and dynamics of four concentrated sulfone-based electrolytes—LiFSA–SL, LiFSA–MSL, LiFSA–DMS, and LiFSA–EMS—at a 1:3 salt-to-solvent ratio, which is representative of the HCE regime. Through detailed MD simulations, we probe solvation structures, van Hove correlation functions, dynamic heterogeneity, and ligand-exchange kinetics to elucidate how solvent symmetry and geometric character influence lithium-ion mobility and hopping dynamics. The four selected solvents differ in both structural symmetry (symmetric vs. asymmetric) and cyclic vs. acyclic topology, allowing us to directly assess the geometric effects on conduction mechanisms. This study provides an atomistically resolved picture of Li^+ conduction in structurally diverse sulfone environments. The novelty of this work lies in (i) utilizing previously developed GA–GPR optimized force fields to accurately capture LiFSA–sulfone interactions across chemically distinct systems and (ii) performing a systematic dissection of the combined effects of molecular symmetry and ring topology on lithium-ion hopping and solvation dynamics in concentrated electrolytes—an aspect that has not been concurrently addressed in earlier literature.

2 | Experimental Section

2.1 | Classical MD Simulations

This study aims to elucidate the role of atomic-level interactions in governing the bulk dynamics and lithium-ion transport in concentrated LiFSA–sulfone mixtures. Given the viscous, ionic-liquid-like nature of these systems, lithium-ion hopping and diffusive motions occur over relatively long timescales [12]. Therefore, extended simulations are required to capture statistically reliable transport characteristics. While ab initio molecular dynamics (AIMD) provides high accuracy, its computational cost limits accessible timescales. To overcome this limitation, we performed classical MD simulations using optimized force fields previously developed and validated by our group against experimental data and AIMD benchmarks [16, 34]. These force fields accurately reproduce structural, thermodynamic, and dynamic properties of LiFSA–sulfone electrolytes.

All simulations were carried out using the GROMACS [35, 36] software package. The total potential energy of the system is expressed as:

$$U_{\text{total}} = \sum_{\text{bonds}} k_b (r - r_0)^2 + \sum_{\text{angles}} k_\theta (\theta - \theta_0)^2 + \sum_{\text{dihedrals}} \sum_{n=0}^{5} C_n \cos^n(\phi)$$

$$+ \sum_{i<j} \left[4\epsilon_{ij} \left(\left(\frac{\sigma_{ij}}{r_{ij}} \right)^{12} - \left(\frac{\sigma_{ij}}{r_{ij}} \right)^{6} \right) + \frac{q_i q_j}{4\pi\epsilon_0 r_{ij}} \right]$$

The bonded parameters (bond stretching, angle bending, and dihedral torsion terms) were adopted from the OPLS-AA force field [32, 33], while the nonbonded parameters—including Lennard-Jones (σ, ϵ) terms and partial charges—were taken from our previously optimized GA-GPR-derived parameter sets for the LiFSA–SL, LiFSA–DMS, LiFSA–EMS, and LiFSA–MSL mixtures [16, 34]. The chemical structures of components are shown in Figure 1.

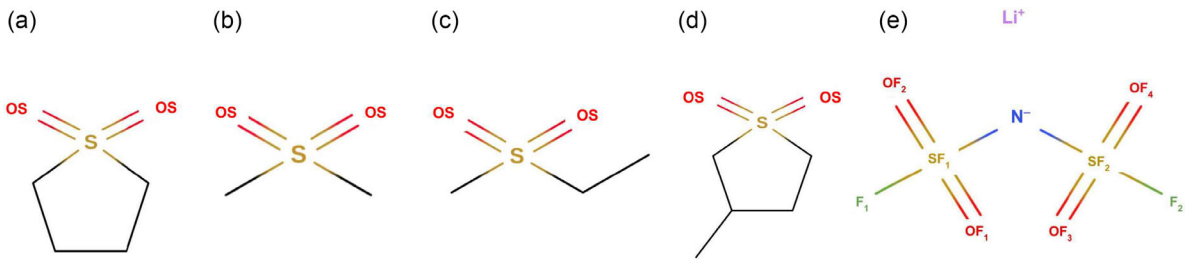

FIGURE 1 | Molecular structures of the electrolytic components studied: (a) sulfolane (SL), (b) dimethyl sulfone (DMS), (c) EMS, (d) 3-methyl sulfolane (MSL), and (e) lithium bis(fluorosulfonyl)imide (LiFSA).

Initial gas-phase geometries of individual molecules were optimized using the M06-2X/aug-cc-pVDZ level of theory in Gaussian09 [37]. The optimized structures were then packed into a cubic simulation box using Packmol [38], containing 160 LiFSA ion pairs and 480 sulfone molecules, corresponding to a 1:3 salt-to-solvent ratio typical of the high-concentration regime. The composition was chosen to ensure consistent molecular densities across systems and to avoid statistical heterogeneity.

2.1.1 | Equilibration Protocol

The equations of motion were integrated with a 1 fs time step using the velocity Verlet algorithm. Nonbonded interactions were computed using the Verlet cutoff scheme, with the neighbor list updated every 20 steps and a cutoff distance of 1.3 nm. Electrostatic interactions were treated with the Smooth Particle Mesh Ewald (SPME) [39] method (SPME implementation in GROMACS), and long-range dispersion corrections were applied to both energy and pressure. Temperature control was achieved using the velocity rescaling thermostat [40], and isotropic pressure coupling was maintained at 1 bar using the Berendsen barostat [41] with a relaxation time of 0.5 ps. Prior to production runs, all systems were energy-minimized and subsequently equilibrated in the isobaric-isothermal (NPT) ensemble for 5 ns at 303 K to obtain well-relaxed configurations. The equilibration process was monitored through the time evolution of potential energy, density, and instantaneous volume. For all electrolyte compositions, both potential energy and density reached stable plateau values within ~1.5 ns, followed by fluctuations around well-defined mean values without any systematic drift, indicating proper thermodynamic equilibration. Representative convergence plots are provided in Figure S1.

2.1.2 | Production Runs

Following equilibration, production simulations were conducted in the canonical (NVT) ensemble for 100 ns at 303 K, using a 1 fs integration time step. Although neat solvents exhibit relatively high melting points, the melting point is significantly depressed upon the addition of LiFSA at high concentration. The LiFSA–sulfone mixtures at comparable compositions have been experimentally prepared and characterized at 303 K [11], confirming that these systems remain in the liquid state. Accordingly, a 1:3 salt-to-solvent molar ratio was adopted for consistent comparison across all mixtures. The trajectory was recorded every 100 fs to capture short-time correlations relevant to lithium-ion hopping and solvation dynamics. This extended simulation duration enabled the collection of statistically robust data to analyze lithium-ion hopping, diffusion behavior, and dynamic heterogeneity across the four mixtures.

2.2 | Structural and Dynamical Analyses

To uncover the microscopic origin of lithium-ion transport and dynamic heterogeneity in concentrated LiFSA–sulfone mixtures, several time-resolved statistical analyses were performed on the equilibrated 100 ns trajectories. These include the van Hove correlation functions [42], non-Gaussian parameter [43–45], residence lengths, and ligand-exchange rates. All analyses were conducted using in-house Python scripts interfaced with GROMACS output files, and averages were computed over all Li^+ ions in each trajectory to ensure statistical reliability.

2.2.1 | Van Hove Correlation Functions

The self and distinct parts of the van Hove correlation function provide quantitative information about lithium-ion motion and the evolution of its local environment over time [12]. The self part [$G_s(r,t)$] describes the probability of finding a lithium ion at a distance r from its initial position after a time t:

$$G_s(r,t) = \frac{\rho}{N}\left\langle \sum_{i=1}^{N} \Delta\left(r - |\mathbf{r}_i(t) - \mathbf{r}_i(0)|\right)\right\rangle \quad (1)$$

where ρ is the number density of Li^+ ions, and N is the total number of Li^+ ions in the system. This function captures the displacement distribution of each ion, reflecting whether its motion is localized or diffusive. The self part was evaluated over 100 ns trajectories using 1, 10, 30, 50, 70, and 90 ns time lags.

The distinct part [$G_d(r,t)$] captures the relative motion of surrounding Li^+ ions with respect to a reference ion and provides insight into structural relaxation and correlated hopping:

$$G_d(r,t) = \frac{\rho}{N}\left\langle \sum_{i=1}^{N}\sum_{j\neq i} \Delta\left(\mathbf{r} - [\mathbf{r}_j(t) - \mathbf{r}_i(0)]\right)\right\rangle \quad (2)$$

where $G_d(r,t)$ represents the temporal evolution of the local environment around the i^{th} Li^+ ion. For this analysis, selected time intervals (1, 10, 30, 50, and 90 ns) were used to probe long-range hopping events and the replacement of lithium ions in their coordination shells.

2.2.2 | Dynamic Heterogeneity

The non-Gaussian parameter [$\alpha_2(t)$] was computed to quantify deviations from Gaussian diffusive behavior [46]. This parameter characterizes the extent of dynamic heterogeneity within the system and highlights the nonuniform mobility of lithium ions:

$$\alpha_2(t) = \frac{3\langle r^4(t)\rangle}{5\langle r^2(t)\rangle^2} - 1 \quad (3)$$

where $\langle r^n(t)\rangle$ represents the n^{th} moment of the Li^+ displacement distribution. The analysis was performed on the 100 ns trajectory with a 100 fs sampling interval to capture deviations from Gaussian dynamics at both short- and long-time scales.

2.2.3 | Hopping Analysis

To quantify the hopping mechanism, the last 20 ns of each trajectory were analyzed to ensure statistical uniformity across all mixtures. Li^+ displacements were computed over consecutive frames, and events exceeding 1.52 Å were identified as hopping events. This threshold was chosen to exclude small-amplitude vibrational fluctuations within the solvation cage. The total number of Li^+ ions participating in hopping is denoted as n_{Li}, while the average hopping distance and average number of hops per participating ion are reported as d_{avg} and n_{hop}, respectively.

2.2.4 | Residence Length

To further dissect the contribution through diffusive migration to lithium-ion motion, a residence length was defined based on the characteristic residence time and Li diffusion coefficient [28]. The residence length [L_{res}] quantifies the average distance traveled by a Li^+ ion within its coordination lifetime:

$$L_{res} = \sqrt{6D_{Li}\tau_{Li-Sol}} \quad (4)$$

where D_{Li} is the diffusion coefficient of Li^+ and τ_{Li-Sol} represents the residence time of Li^+ within its solvation environment.

2.2.5 | Ligand-Exchange Dynamics

The ligand-exchange rate measures the temporal stability of Li–O interactions originating from solvent or anion coordination [29]. To compute this, all Li–O interactions were monitored in 1 ns time windows throughout the 100 ns trajectory, which was divided into ten 1 ns blocks for statistical averaging. A binary binding function, [$S(r_i(t),r_j(t),t)$], was defined as:

$$S(r_i(t), r_j(t), t) = \begin{cases} 1, & |r_j(t) - r_i(t)| > l_0 \\ 0, & |r_j(t) - r_i(t)| > l_0 \end{cases} \quad (5)$$

where l_0 denotes the Li–O cutoff distance defining a coordination bond. The cutoff distance l_0 was determined from the corresponding radial distribution functions (Figure S2), where the first peak decays to zero at ~2.5 Å in all systems. Accordingly, $l_0 = 2.5$ Å was used to define coordinated oxygen atoms in the exchange dynamics calculations. The binary binding function $S(t)$ was defined for each Li–O_S and Li–O_F pair, where $S(t) = 1$ when the Li–O distance is within the first coordination shell and 0 otherwise. The exchange rate (k_{Li-O}) was calculated as the average number of coordination entry and exit events per Li^+ per nanosecond. The residence time (τ_{Li-O}) was determined from the average duration of continuous binding intervals (difference between "on" and "off" times), without multi-exponential fitting of time-correlation functions.

2.3 | Metadynamics

Metadynamics simulations were carried out in GROMACS using the PLUMED [47] plugin to obtain 1D and 2D free-energy profiles associated with Li^+ solvation and exchange. Equilibrated configurations from classical MD trajectories were used as starting points. Simulations were performed in the NVT ensemble at 303 K for 3 ns, with Gaussian hills of 1.2 kJ mol^{-1} height and 0.05 width deposited every 500 fs (bias factor = 10).

The 1D metadynamics tracked the coordination number between Li^+ and solvent oxygen atoms (Li–O_S), while the 2D metadynamics simultaneously biased the Li–O_S and Li–O_F (anion oxygen) coordination numbers to capture the interplay between solvation and anion exchange. The coordination number was computed using the continuous switching function implemented in PLUMED, allowing for noninteger values. Free-energy surfaces (FES) were reconstructed from the accumulated bias potentials to map the preferred coordination states and transition barriers governing Li^+ hopping dynamics.

3 | Results and Discussion

The present study aims to elucidate the microscopic mechanisms by which organic sulfone additives enhance the ionic conductivity of highly concentrated LiFSA-based electrolytes. In such electrolytic systems, ionic conduction arises from a complex interplay between lithium-ion diffusion and hopping processes, both of which are sensitive to the local solvation structure and dynamic environment. The chosen additives—all members of the sulfone family—exert distinct influences on these processes due to differences in their molecular topology and asymmetry. Understanding the chemical nature and structural effects of these additives is crucial for elucidating how they influence lithium dynamics and, consequently, the overall transport behavior of the electrolyte. To gain quantitative insight into these mechanisms, we first examine the temporal evolution of lithium displacements through the self part of the van Hove correlation function [$G_s(r,t)$], which captures the fundamental features of ion motion across different spatial and temporal scales.

The self part of the van Hove correlation function, $G_s(r,t)$, traces the displacement probability of lithium ions over different timescales, thereby revealing the extent and nature of their microscopic mobility (Figure 2). At short lag times (1 ns), all mixtures display a narrow, intense peak centered near zero displacement, signifying caged Li^+ motion confined within the local solvation network. This localization reflects the intense ion–dipole interactions characteristic of concentrated LiFSA–sulfone mixtures. Clear differences emerge among the electrolytes as the correlation time increases (10–90 ns). EMS exhibits a pronounced broadening and development of long tails (Figure 2c), indicative

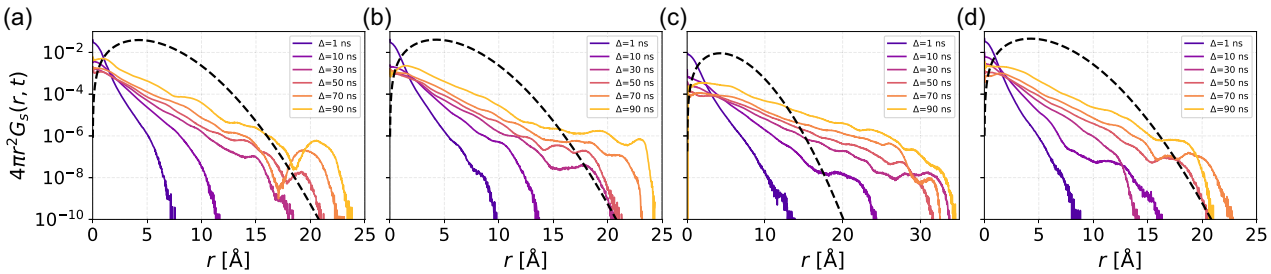

FIGURE 2 | Radial self van Hove correlation function, $G_s(r,t)$ (Equation ((1))), for Li^+ ions at time lags of 1, 10, 30, 50, 70, and 90 ns in four concentrated LiFSA–sulfone electrolytes: (a) LiFSA–SL, (b) LiFSA–DMS, (c) LiFSA–EMS, and (d) LiFSA–MSL. The evolution of $G_s(r,t)$ illustrates the transition from localized (caged) motion to long-range diffusive or hopping dynamics, varying with the molecular topology of the additive. The black dotted lines depict an ideal Gaussian distribution for the purely diffusive motion of Li^+ ions.

of enhanced long-range motion and frequent hopping transitions between solvation cages. Despite being cyclic, MSL also shows significant broadening (Figure 2d), suggesting that molecular asymmetry compensates for the structural rigidity of its ring. In contrast, SL and DMS retain sharper profiles and slower decay of the central peak, consistent with more restricted Li^+ mobility (Figure 2a,b). Among these, SL—being both symmetric and cyclic—shows the strongest localization, with lithium ions remaining caged over extended timescales. While the mean hopping amplitude remains comparable across systems, the proportion of ions participating in long-range hops varies strongly, mirroring the role of molecular asymmetry and flexibility in facilitating Li^+ motion. The secondary peak observed in the self part of the van Hove function reflects dynamic heterogeneity associated with transient cage escape rather than purely discrete long-range hopping. In SL, the stronger and more persistent solvation cage leads to temporally separated caged and mobile populations, resulting in a more pronounced secondary feature at longer times. In contrast, although EMS and MSL exhibit more frequent hopping events, the exchange processes are more continuous and less temporally separated, producing a smoother displacement distribution and a less distinct secondary peak. For comparison, the ideal Gaussian distributions corresponding to purely diffusive motion are also included, highlighting the deviation from Gaussian behavior and confirming the presence of heterogeneous dynamics.

The distinct van Hove function, $G_d(r,t)$, captures the temporal evolution of spatial correlations among different lithium ions and provides insights into how local ionic neighborhoods rearrange over time (Figure 3). At early time lags, all systems exhibit a well-defined peak in the Li–Li distinct correlation, corresponding to the characteristic nearest neighbor cation separation and indicating strong short-time dynamical correlation. This reflects a structured arrangement of neighboring Li^+ ions undergoing correlated motion within a transient cage. At longer time lags, the distortion and eventual relaxation of this cationic cage lead to peak broadening and attenuation, signifying loss of correlation and the emergence of dynamic heterogeneity. The rate and extent of this decay differ markedly across the mixtures. EMS exhibits the most rapid attenuation of the primary peak (Figure 3c), implying facile restructuring of Li–Li correlations and highly labile ionic environments. MSL shows a similar, though slightly slower, relaxation trend (Figure 3d). In contrast, SL maintains persistent structural correlations over tens of nanoseconds, indicating slow reorganization and restricted lithium exchange (Figure 3a). DMS lies intermediate between the two regimes (Figure 3b). Taken together, the self and distinct van Hove analyses confirm that molecular asymmetry—particularly in EMS and MSL—promotes rapid reorganization of lithium solvation shells, thereby enabling efficient hopping-mediated transport in concentrated sulfone systems. A similar observation was reported from the distinct van Hove analysis for Li–O interactions, included in the supporting information.

To further quantify deviations from homogeneous diffusive behavior, we calculated the non-Gaussian parameter, $\alpha_2(t)$, which characterizes the spread in individual ion displacements relative to Gaussian diffusion (Figure 4). Among the four systems, DMS exhibits the most prominent peak in α_2, signifying pronounced dynamic heterogeneity and intermittent hopping events, where a subset of Li^+ ions undergoes rapid transitions, while others remain immobilized. The secondary peak observed in the non-Gaussian parameter of Li^+ in DMS originates from pronounced dynamic heterogeneity associated with intermittent hopping events. In DMS, the relatively labile coordination environment enables cage escape followed by retrapping at nearby sites, leading to two temporally separated dynamical regimes. SL and MSL display moderate non-Gaussianity, suggesting coexistence of both mobile and caged ion populations. In contrast, EMS maintains relatively low α_2 values across all timescales, implying that its enhanced transport arises from a more

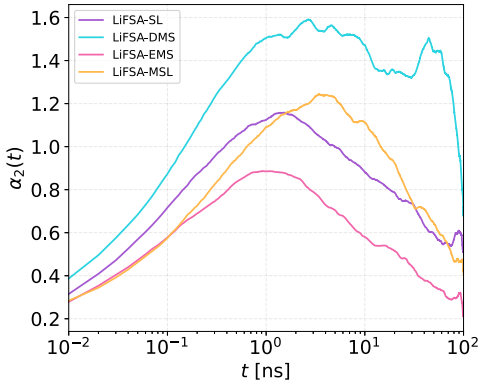

FIGURE 4 | Non-Gaussian parameter [$\alpha_2(t)$] as a function of simulation time (up to 100 ns) for Li^+ ions in the four LiFSA–sulfone electrolytes. The evolution of $\alpha_2(t)$ highlights deviations from purely diffusive behavior, reflecting the extent and timescale of dynamic heterogeneity associated with lithium hopping and cage relaxation.

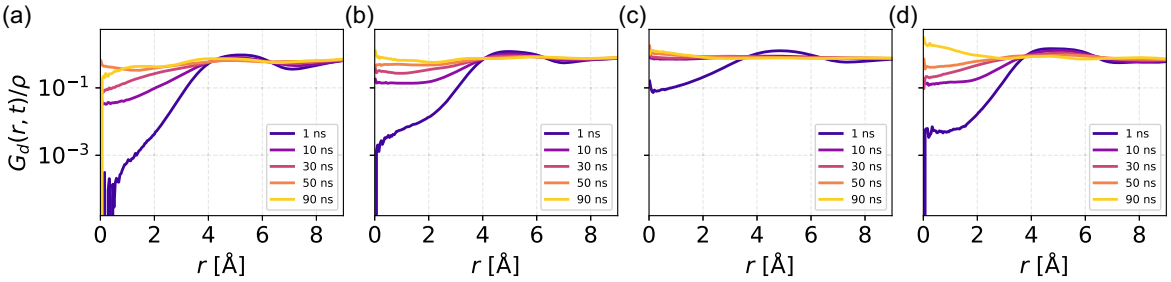

FIGURE 3 | Radial distinct van Hove correlation function, $G_d(r,t)$ (Equation ((2))), for Li^+ ions at time lags of 1, 10, 30, 50, and 90 ns in four concentrated LiFSA–sulfone electrolytes: (a) LiFSA–SL, (b) LiFSA–DMS, (c) LiFSA–EMS, and (d) LiFSA–MSL. The decay of the primary Li–Li correlation peak with increasing time lag reflects the structural relaxation and exchange rate among lithium environments, which vary with the molecular topology and symmetry of the additives.

homogeneous and collective hopping mechanism rather than isolated, sporadic events. This distinction is critical: high ionic mobility in EMS is achieved through synchronized reorganization of solvation networks, whereas in DMS and SL, transport proceeds via localized, heterogeneous rearrangements. The timescales associated with the $\alpha_2(t)$ maxima correlate well with those inferred from the van Hove analyses, reinforcing the consistency of the observed dynamics.

Quantitative characterization of hopping events further elucidates the observed mobility differences (Table 1). The computed hopping data reveal that EMS supports the most significant number of hops and the longest total hopping distance, underscoring its superior capacity for Li^+ migration. MSL also exhibits high hopping activity, driven by its asymmetric molecular architecture that facilitates frequent solvation rearrangements despite the inherent rigidity of its cyclic backbone. DMS exhibits moderate hopping behavior, with a smaller subset of ions engaging in long-range motion, whereas SL displays the fewest hopping events, consistent with its strong and persistent Li–O_S coordination network. Notably, the average displacement per hop remains nearly constant across all systems (1.58–1.61 Å), suggesting that the elementary hopping step is governed by the characteristic Li–O_S coordination distance. Thus, the differences in overall conductivity arise primarily from the frequency and participation fraction of hopping ions rather than the magnitude of individual hopping steps.

TABLE 1 | Quantitative summary of Li^+ hopping statistics over a 20 ns simulation window for the four LiFSA–sulfone electrolytes.

Mixtures	n_{Li}	d_{avg}, Å	n_{hop}	d_{tot}, Å
LiFSA–SL	4	1.59	4	6.37
LiFSA-DMS	30	1.61	37	59.41
LiFSA-EMS	28	1.59	47	74.85
LiFSA-MSL	32	1.58	40	63.20

Note: The table lists the number of participating Li^+ ions (n_{Li}, with displacement > 1.52 Å per hop), average displacement per hop (d_{avg}), total number of hops (n_{hop}), and cumulative hopping distance (d_{tot}), providing a comparative measure of lithium mobility across the different solvent environments.

The distribution of hopping distances across lithium ions offers further insight into the collective nature of ion motion (Figure 5). In EMS and DMS, the total hopping distances are widely distributed over a large number of ions, indicating broad participation in the transport process (Figure 5a). EMS again demonstrates the highest number of actively hopping ions, coupled with substantial total displacement, reinforcing its role as the most dynamically labile system. MSL mirrors this collective participation, with comparable distribution breadth and total hopping distance, signifying that asymmetry can effectively enhance ion dynamics even within cyclic frameworks (Figure 5b). SL, by contrast, exhibits limited activity, with most Li^+ ions remaining immobile throughout the simulation. The nearly identical mean hopping distances across all systems confirm that solvent geometry and symmetry predominantly influence the frequency and cooperativity of hopping, not its characteristic scale (Figure 5c).

The migration profiles of representative Li^+ ions in the four LiFSA–sulfone electrolytes offer a direct microscopic view of lithium transport and the underlying hopping dynamics (Figure 6). Each trajectory traces the time-dependent displacement of a single ion, thereby capturing both the magnitude of motion and the kinetic character of successive solvation-site exchanges. In LiFSA–DMS (Figure 6b), the time series displays pronounced stepwise increments in D_{Li}, separated by extended plateaus. Each abrupt rise corresponds to a distinct hopping event, where the ion escapes a local coordination cage—typically stabilized by

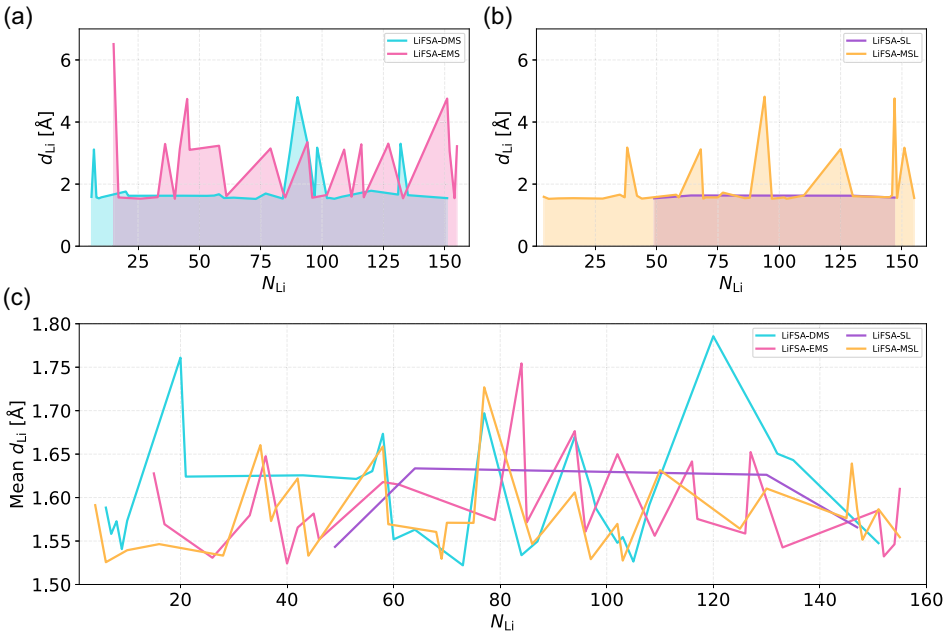

FIGURE 5 | Distribution of Li^+ hopping distances across individual ion indices for LiFSA–sulfone mixtures. Panels (a) and (b) depict the total hopping distance (y-axis) of each Li^+ ion (x-axis) for acyclic and cyclic sulfones, respectively; the shaded region highlights the cumulative hopping distance of all participating ions. Panel (c) shows the mean hopping distance per Li^+ ion, illustrating the variation in ion participation and mobility among different electrolyte systems.

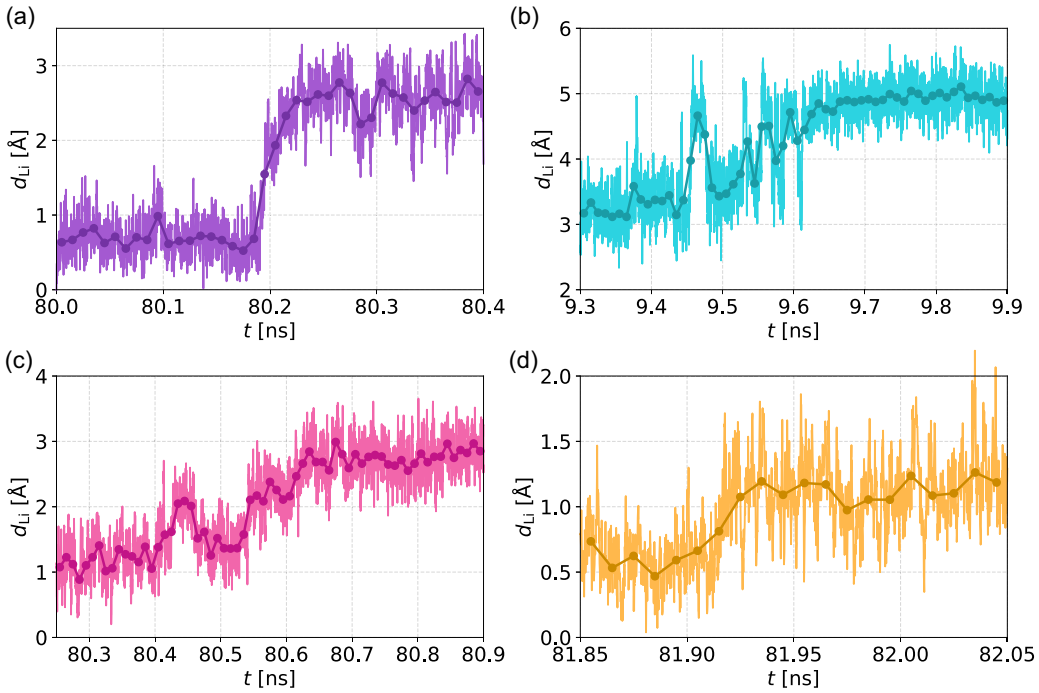

FIGURE 6 | Representative trajectories of Li^+ cation migration in LiFSA–sulfone electrolytic mixtures: (a) LiFSA–SL, (b) LiFSA–DMS, (c) LiFSA–EMS, and (d) LiFSA–MSL. Each plot depicts the time-dependent displacement of a single Li^+ ion over the simulation window, illustrating distinct hopping behaviors and confinement characteristics arising from the molecular structure of the sulfone additives.

sulfone oxygen atoms—and relocates to a neighboring solvation site, often traversing ∼3 Å . The alternation between stable plateaus and rapid transitions reflects a rugged free-energy landscape: Li^+ experiences transient trapping within deep coordination wells, followed by barrier crossing facilitated by collective solvent reorientation or anion exchange. This pattern evidences pronounced dynamic heterogeneity, characterized by intermittent, nonuniform mobility.

In LiFSA–SL (Figure 6a), the trajectory shows minimal amplitude and nearly continuous confinement, with only a single observable hop throughout the investigated window. The symmetric cyclic architecture of SL imposes steric rigidity and reduces the flexibility of coordinating oxygens, thereby strengthening ion–dipole interactions and hindering cage rearrangement. Consequently, Li^+ remains largely immobilized within a persistent solvation shell, exhibiting localized vibrational motion rather than translational migration. In stark contrast, LiFSA–EMS (Figure 6c) demonstrates frequent and uniform hopping behavior. The trace reveals numerous stepwise displacements of comparable magnitude, each separated by short plateaus. These features indicate facile and repeated coordination exchange, consistent with a highly labile solvation environment. The presence of asymmetric sulfone substituents in EMS enhances molecular flexibility and dipole moment distribution, enabling rapid reorganization of solvent molecules around the migrating cation. This leads to collective and homogeneous lithium transport, where motion is distributed evenly across time and ions rather than concentrated in rare events. For LiFSA–MSL (Figure 6d), the migration pattern occupies an intermediate regime between SL and EMS. Multiple hops of variable amplitude occur, separated by intervals of partial confinement. The asymmetric cyclic framework of MSL relaxes the geometric rigidity of SL, allowing occasional reorientation of coordinating groups and facilitating moderate hopping events. However, the retention of a cyclic core still imposes steric constraints, leading to intermittent trapping within specific solvation motifs.

Collectively, these single-ion trajectories provide a mechanistic window into the interplay between solvent topology, coordination dynamics, and energetic landscape. SL's symmetric cyclic geometry enforces rigid, localized solvation; DMS and MSL exhibit intermittent cage-breaking and reformation, revealing heterogeneous kinetics; while EMS enables fast and spatially uniform solvation exchange that underpins enhanced lithium mobility. These observations reinforce ensemble analyses, highlighting how molecular architecture governs the microscopic mechanism of ion transport in concentrated LiFSA–sulfone electrolytes.

The ligand-exchange data (Table 2) further elucidate the molecular underpinnings of lithium transport by quantifying the dynamic stability of Li^+ coordination with solvent and anion species. Together with the hopping and migration analyses discussed earlier, these results refine our understanding of how local solvation structures evolve in response to molecular topology and symmetry.

Focusing first on the Li–O_S interactions, the data reveal pronounced contrasts across the sulfone series. In LiFSA–SL, lithium ions undergo solvent exchange at an exceptionally slow rate, with residence times exceeding half a nanosecond—nearly an order of magnitude longer than in any other mixture. This persistent coordination implies a highly stable and structured solvation environment, consistent with the rigid, symmetric cyclic architecture of SL, which restricts local configurational rearrangements. In contrast, the acyclic sulfones (DMS and EMS) and the asymmetric cyclic analog (MSL) exhibit far more labile solvation shells. Here, frequent ligand exchange and shorter residence times point to rapidly fluctuating coordination networks

TABLE 2 | Lithium–oxygen (Li–O) exchange kinetics showing the average number of exchanges per Li^+ per nanosecond (k_{Li-O}), mean residence time (τ_{Li-O}) of coordinating solvent and anion oxygen atoms for different LiFSA–sulfone mixtures.

	Li–O_S	Coordination	Li–O_F	Coordination
Mixtures	k_{Li-OS}	τ_{Li-O_S}, ps	k_{Li-OF}	τ_{Li-O_F}, ps
LiFSA–SL	1.87	573.11	38.78	19.86
LiFSA-DMS	21.56	47.48	34.38	26.31
LiFSA-EMS	84.75	11.54	30.20	30.80
LiFSA-MSL	24.82	40.15	35.19	26.26

that allow Li^+ to migrate via continuous renewal of solvent partners. Among them, EMS stands out as the most dynamic system, with the fastest exchange and shortest residence, underscoring its flexible and disordered solvation landscape.

The Li–O_F exchange data present a complementary perspective on lithium–anion interactions. Across all mixtures, anion coordination is considerably more transient than solvent coordination, especially in LiFSA–SL. This indicates that FSA anions engage in fleeting, rapidly renewing associations with lithium, reflecting the dynamic nature of ion-pairing under high-concentration conditions. Although the overall variation between systems is less pronounced than for solvent coordination, subtle trends remain informative. SL displays the most solvent-selective behavior, characterized by strong, long-lived solvent coordination and relatively weak anion association. In contrast, MSL shows comparably strong participation from both solvent and anion oxygens—consistent with a more congested and competitive coordination environment arising from its asymmetric cyclic structure. DMS and EMS occupy an intermediate regime, where lithium alternates rapidly between solvent and anion coordination in a highly labile fashion. Although DMS, EMS, and MSL exhibit longer Li—O_F lifetimes, hopping remains active due to intermittent coordination exchange within the first shell. Thus, persistent local interactions coexist with relay-type structural rearrangements, enabling frequent hopping events despite stronger Coulombic associations.

These distinctions define two dominant solvation modes that coexist across the series. SL embodies a "solvent-dominant" regime, where lithium mobility occurs within stable, well-organized solvation shells conducive to coherent, vehicular diffusion. MSL, in contrast, represents a "mixed-coordination" regime, where solvent and anion compete dynamically for lithium coordination sites, promoting local crowding and potentially enhancing microviscous resistance. The acyclic sulfones (DMS and EMS) bridge these extremes, offering highly dynamic, rapidly exchanging environments that enable facile site-to-site hopping while maintaining overall solvation flexibility.

Collectively, these findings reinforce the emerging mechanistic picture from the earlier migration and hopping analyses: solvent topology and molecular asymmetry dictate the balance between structural rigidity and dynamical renewal within the lithium solvation environment. The persistence or lability of these local interactions directly influences the macroscopic properties of the mixtures—linking the observed differences in viscosity and conductivity to the fundamental kinetics of coordination exchange.

To further substantiate the mechanistic picture emerging from the ligand-exchange analysis, we performed well-tempered metadynamics simulations to probe the free-energy landscape governing lithium coordination dynamics. Two collective-variable (CV) formulations were employed: (i) a 1D free-energy profile as a function of the Li–O_S coordination number, and (ii) a 2D FES constructed over Li–O_S and Li–O_F coordination numbers. These analyses provide complementary thermodynamic insights into the stability and competition between solvent and anion coordination, expanding upon the kinetic trends discussed earlier.

The 1D free-energy profiles reveal that SL strongly favors solvation states with higher Li–O_S coordination, indicating the thermodynamic preference for a multi-ligand solvent-rich shell (Figure 7). This finding corroborates the long residence times and slow solvent exchange observed in the kinetic data, as well as the structured, persistent coordination seen in radial distribution functions. The deep minimum at high coordination numbers confirms the stability of these configurations and underscores the rigidity of the solvation cage that defines lithium transport in SL. In contrast, the 2D FES (Figure 8) demonstrates distinct solvation topographies across the sulfone series. SL features a well-defined basin localized at high Li–O_S and low Li–O_F values, confirming a solvent-dominant coordination environment with minimal anion participation. This corresponds to a vehicular-type transport mechanism, wherein Li^+ ions migrate in concert with their intact solvation shells.

MSL, on the other hand, exhibits a broader basin extending toward higher Li–O_F values, revealing significant participation

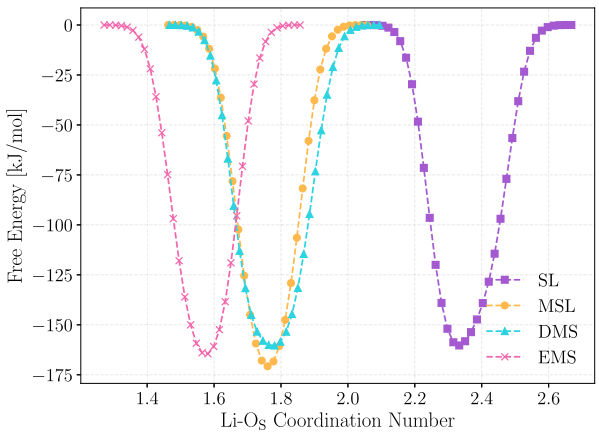

FIGURE 7 | 1D free-energy profiles of Li^+ solvation obtained from metadynamics simulations using the Li–O_S coordination number as the collective variable. The profiles reveal solvent-dependent stabilization of Li–O_S coordination states, highlighting stronger solvent binding in SL compared to other sulfone systems.

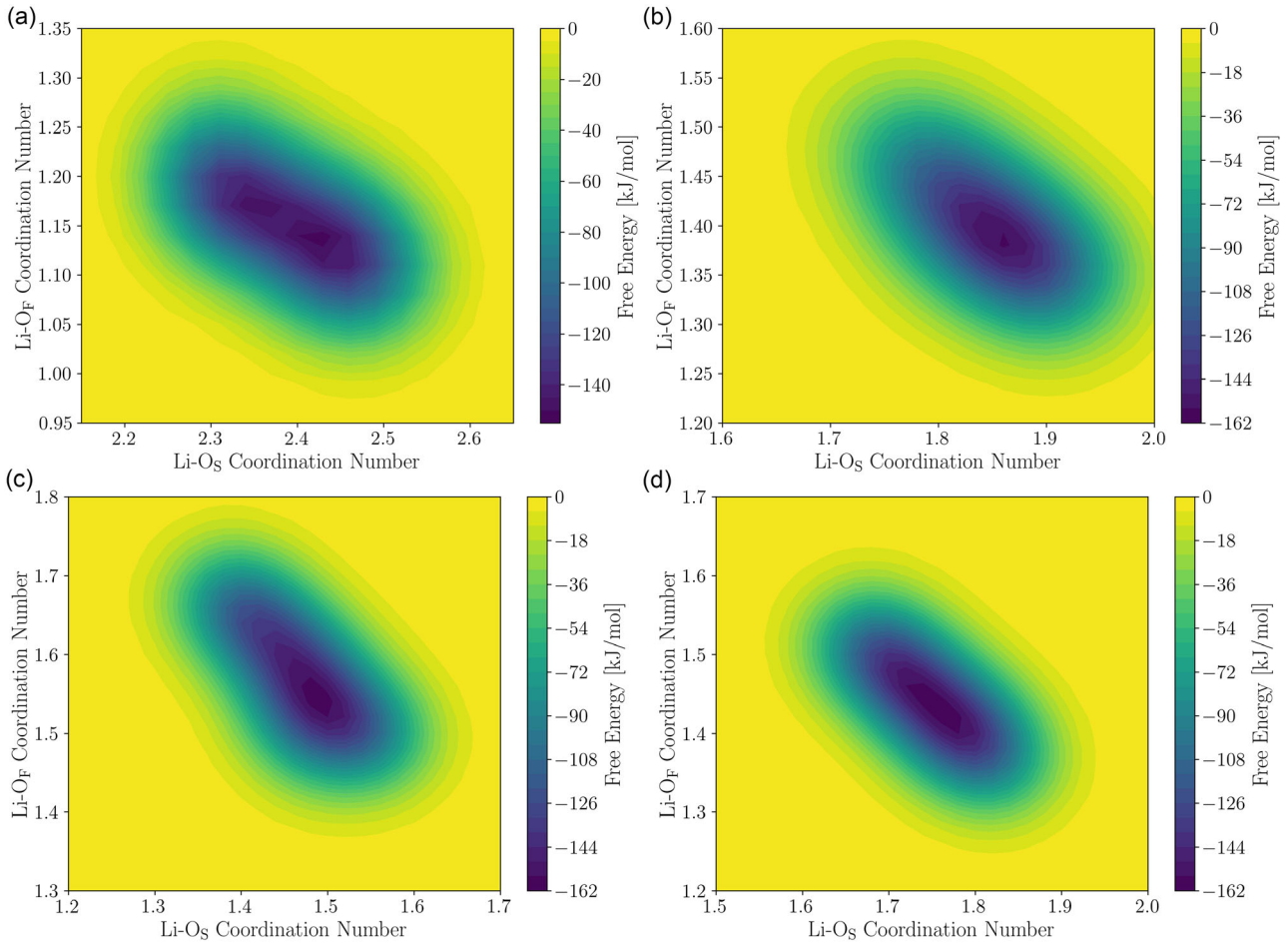

FIGURE 8 | 2D FES projected along the Li–O_S and Li–O_F coordination numbers for (a) SL, (b) DMS, (c) EMS, and (d) MSL electrolytes. The surfaces illustrate distinct solvation topographies—from solvent-dominated basins in SL to broader, mixed, or anion-involved coordination landscapes in MSL, DMS, and EMS—reflecting the transition from vehicular to hopping lithium transport mechanisms.

of both solvent and anion oxygens in lithium coordination. This mixed-coordination state suggests a more complex solvation environment where transient ion pairing and solvent reorganization coexist, contributing to moderate exchange rates and intermediate mobility. The competition between solvent and anion coordination likely introduces local frustration and transient caging effects, consistent with the elevated viscosity and partially hindered lithium transport observed for this system.

DMS and EMS display much flatter and more delocalized FES, characterized by multiple shallow minima distributed over a range of Li–O_S and Li–O_F combinations. These landscapes reflect highly labile coordination equilibria, where lithium ions rapidly interchange between solvent and anion partners. The small free-energy barriers between states enable frequent reorganization of solvation shells, facilitating dynamic hopping events. Such thermodynamic flexibility complements the kinetic observations of high ligand-exchange rates and short residence times, establishing DMS and EMS as paradigms of hopping-dominated lithium transport in highly dynamic solvation environments.

Taken together, the metadynamics results integrate thermodynamic and kinetic perspectives to present a unified picture of lithium coordination and migration in concentrated LiFSA–sulfone electrolytes. SL represents a solvent-stabilized regime with deep, well-defined basins and persistent coordination favoring coherent vehicular motion. DMS and EMS occupy the opposite end, where shallow, interconnected minima correspond to facile exchange and hopping transport. With its dual coordination to solvent and anion, MSL bridges these extremes through a mixed mechanism that strikes a balance between stability and flexibility. These insights reinforce that the interplay between solvation thermodynamics and coordination dynamics governs lithium mobility at the molecular scale. By tuning solvent topology and symmetry, one can modulate the relative contributions of vehicular and hopping mechanisms—an essential design handle for optimizing ionic conductivity in next-generation concentrated sulfone-based electrolytes.

The temporal evolution of the Li–O_S coordination number (Figure 9) further substantiates the thermodynamic and kinetic trends inferred from the free-energy landscapes. In SL, the coordination number remains nearly constant with minimal fluctuations, as reflected by the narrow shaded band, signifying a highly stable and persistent solvation shell. This steady coordination correlates with the deep free-energy minima and slow ligand-exchange kinetics, confirming the presence of a strongly bound, solvent-dominated solvation environment. In contrast, MSL exhibits moderate fluctuations around a high mean coordination number, indicating occasional solvent rearrangements and transient coordination changes—consistent with its mixed solvation

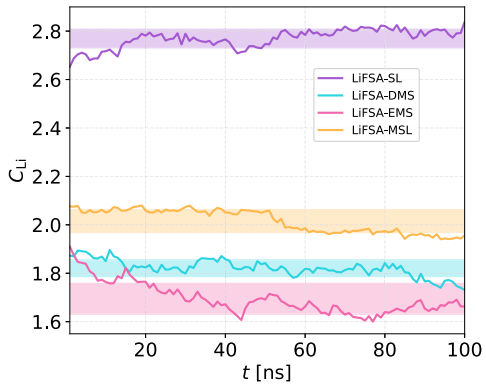

FIGURE 9 | Time evolution of the Li–O_S coordination number from classical MD simulations. The shaded regions denote standard deviations, reflecting the extent of coordination fluctuations in each electrolyte mixture.

behavior and intermediate kinetic characteristics. DMS and EMS, however, display pronounced temporal variability and broader standard-deviation bands, reflecting a highly labile solvation environment with frequent ligand exchanges and reorganization of the coordination shell. These dynamic fluctuations mirror the shallow free-energy basins and lower energy barriers for solvation rearrangement, which is characteristic of hopping-dominated transport. Overall, the coordination number dynamics complement the free-energy and exchange-rate analyses, collectively illustrating that SL stabilizes a rigid, long-lived solvation structure conducive to vehicular diffusion, while DMS and EMS promote fast-exchanging, flexible solvation conducive to hopping transport. MSL resides between these regimes, striking a balance between structural stability and dynamic adaptability.

The residence length (Table 3) provides a unified perspective that connects lithium diffusion, residence time, and molecular dimensions, thereby enabling the quantitative analysis of vehicular transport modes. It essentially quantifies the relative displacement a lithium ion achieves during the lifetime of its solvation shell. Among the four mixtures, SL exhibits the highest residence length by a margin, although its diffusion coefficient is comparatively low. The large value (0.74 Å) arises from an exceptionally long solvent residence time of about ∼573 ps, which allows lithium ions to traverse distances exceeding the dimension of the solvent molecule (3.25 Å) during each coordination event. Although the SL system exhibits the lowest number of hopping events and the longest Li–O_S residence time, Li^+ transport is not strictly limited to purely vehicular motion. The strong solvation cage predominantly favors vehicular diffusion; however, infrequent solvent-exchange events still occur, enabling occasional but finite jumps. Thus, while hopping is minimal compared to the other mixtures, its presence indicates a cooperative crossover in which rare exchange-mediated events coexist with dominant vehicular motion. This observation suggests that lithium in SL is not limited to purely vehicular motion with its solvent cage but instead performs infrequent yet substantial jumps, indicative of a hybrid transport regime. The strong, long-lived solvation shell established earlier, as determined by radial distribution function (RDF) and metadynamics analyses, thus coexists with occasional large-scale hopping events, reflecting a cooperative crossover from vehicular to hopping behavior.

TABLE 3 | Calculated residence lengths (L_{res}) for LiFSA–sulfone mixtures, combining lithium diffusion coefficients ($D_{Li} \times 10^{-7}$ cm^2/s), solvent residence times (τ_{Li-SOL}), and molecular dimensions to elucidate the balance between vehicular and hopping transport mechanisms.

Mixtures	D_{Li} [16]	τ_{Li-SOL} (ps)	L_{res}, Å
LiFSA–SL	0.16	573.11	0.74
LiFSA-DMS	0.18	47.48	0.23
LiFSA-EMS	0.52	11.54	0.19
LiFSA-MSL	0.13	40.15	0.18

In contrast, DMS and EMS, while exhibiting higher diffusivities (particularly EMS at 0.52 shown in Table 3), show much lower residence length (0.23 and 0.19 Å, respectively). Their short residence times (∼47 and ∼11 ps, respectively) indicate that lithium frequently exchanges coordinating solvent molecules, consistent with a highly labile solvation shell. However, because each coordination event is brief and the solvent molecules are relatively larger, the effective displacement per coordination period remains small. As a result, lithium motion in these mixtures is dominated by fast, localized hopping events rather than long-range correlated transport. This dynamic aligns with the flatter FES and broad coordination number fluctuations observed earlier, which indicate low energetic barriers and rapid ligand reorganization.

MSL, on the other hand, shows the smallest residence length (0.18 Å), consistent with its lowest lithium diffusivity and relatively large solvent size (3.76 Å). Although the residence time (∼40 ps) suggests moderate exchange dynamics, the strong dual coordination of lithium to both solvent and anion species imposes spatial constraints on ion motion. These interactions likely generate a locally crowded coordination shell that suppresses long-range displacement despite frequent ligand renewal. Such restricted hopping behavior aligns with overall lower ionic mobility and a more viscous environment in the LiFSA–MSL mixture.

The residence length analysis complements the kinetic and thermodynamic insights from exchange dynamics and FES. The high residence length in SL reflects long-lived solvent binding with occasional large displacements—an indicator of coherent vehicular motion with intermittent hopping. DMS and EMS exhibit the opposite limit: fast, frequent ligand exchanges with small spatial displacements, consistent with a continuous hopping-dominated mechanism. MSL lies between these extremes, where dual coordination and steric constraints hinder transport despite moderate exchange activity. Overall, the residence length serves as a bridge connecting the microscopic coordination dynamics with macroscopic lithium mobility. It highlights how the interplay between residence time, diffusion, and solvent structure determines whether lithium transport occurs through stable, coordinated vehicular motion or rapidly fluctuating, short-range hopping within dynamically evolving solvation environments.

The integrated spider plot (Figure 10) provides a unifying perspective on lithium-ion transport by consolidating key descriptors—residence length, ligand-exchange kinetics, Li–O_S coordination, diffusion coefficients (Table 3), ionic conductivity, and viscosity (Table S1)—into a single multidimensional

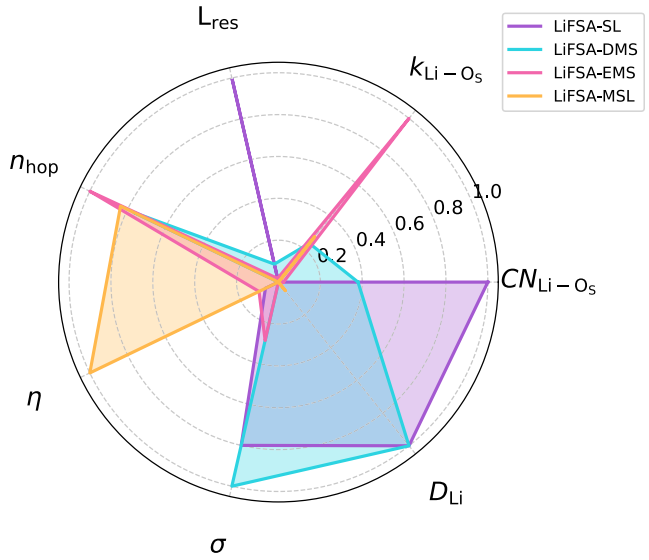

FIGURE 10 | Spider plot summarizing key structural, kinetic, and transport descriptors for LiFSA–sulfone electrolytes, including total Li hops (n_{hop}), residence length (L_{res}), ligand-exchange rate (k_{Li-OS}), Li–O_S coordination number (CN_{Li-OS}), Experimental lithium diffusivity (D_{Li}) [11], ionic conductivity (σ), and viscosity (η). The plot illustrates the interdependence between microscopic solvation dynamics and macroscopic ion-transport properties. Each physical quantity was independently normalized using min–max scaling based on its minimum and maximum values across the studied systems. Specifically, the scaled value was computed so that 0 corresponds to the minimum and 1 to the maximum in that dataset.

framework. It captures how subtle variations in the microscopic solvation structure propagate upward to shape the macroscopic transport properties across the LiFSA–sulfone electrolytes. SL and DMS emerge at one end of the spectrum, characterized by strongly coordinated lithium solvation shells with long solvent residence times and low exchange rates. These systems combine moderate diffusion with relatively high conductivity and low viscosity, reflecting an efficient balance between structural stability and dynamic mobility. In particular, SL stands out with the highest residence length, suggesting that lithium ions, while tightly solvated, can move coherently over distances exceeding the dimensions of the solvent during their residence time. This indicates a hybrid mechanism where vehicular transport [28] predominates but is punctuated by intermittent hopping events—consistent with the deep free-energy minima and narrow coordination number fluctuations observed earlier.

At the opposite end, EMS and MSL exhibit high ligand-exchange rates and short residence times, signaling labile and frequently reorganizing solvation shells. These dynamically flexible environments facilitate frequent, short-range hopping of lithium ions, as evidenced by their higher diffusion coefficients (EMS), but lower conductivities and elevated viscosities. Here, the rapid local reorganization lowers the energetic barriers for hopping yet simultaneously increases solvent friction and structural disorder, thereby reducing the long-range transport efficiency. The lower residence length confirms that lithium motion in these systems is dominated by short, localized hops within transient coordination cages. The coordination number data reinforce this hierarchy: SL maintains a stable, high Li–O_S coordination and DMS displays moderate stability with partial solvent exchange, while EMS and MSL show broad coordination fluctuations consistent with dynamic, heterogeneous solvation environments.

Altogether, the spider plot captures the essence of lithium transport in these concentrated sulfone systems as a continuum between two regimes—one governed by long-lived, coherent vehicular motion (SL-like) and another dominated by rapidly fluctuating, hopping-mediated dynamics (EMS/MSL-like). The intricate balance between solvation stability, exchange kinetics, and solvent structure thus dictates whether lithium motion is smooth and collective or fragmented and stochastic. This integrated view unifies the microscopic and macroscopic perspectives, highlighting that the rational tuning of solvent topology and coordination energetics offers a powerful lever for optimizing ion-transport efficiency in advanced lithium-ion battery electrolytes.

4 | Conclusion

This work presents a comprehensive molecular-level understanding of lithium-ion transport in LiFSA–sulfone electrolytes by integrating classical MD, metadynamics free-energy sampling, and kinetic analyses. Through systematic comparison across cyclic (SL, MSL) and acyclic (DMS, EMS) sulfones, we unravel how subtle variations in solvent topology and coordination dynamics dictate the balance between vehicular and hopping transport mechanisms.

SL emerges as a prototypical system characterized by a stable, multi-ligand solvation shell, slow ligand exchange, and residence length—features that promote coherent, vehicular-like lithium motion within a low-viscosity environment. In contrast, EMS and MSL exhibit labile, dynamically fluctuating solvation environments with rapid ligand exchange and broad free-energy basins, which foster frequent hopping events but also introduce structural disorder that elevates viscosity and limits macroscopic conductivity. DMS occupies an intermediate regime, balancing moderate exchange activity with stable coordination.

Metadynamics simulations provide thermodynamic validation of these distinct solvation modes, revealing deep, solvent-dominated free-energy minima for SL and mixed solvent–anion coordination in MSL, while DMS and EMS display broad, low-barrier landscapes consistent with facile solvation reorganization. The integrated hopping analysis, residence length, and spider plot analyses further link microscopic solvation stability and kinetic flexibility to macroscopic transport observables, establishing a unified framework that connects structure, dynamics, and function.

This study elucidates how lithium-ion mobility in concentrated sulfone electrolytes is influenced by a delicate interplay between solvation shell stability, ligand-exchange kinetics, and solvent symmetry. These insights not only rationalize the observed diversity in transport behavior but also provide guiding principles for the molecular design of next-generation electrolytes that balance stability and mobility for high-performance LIBs.

Author Contributions

AM conceived the problem. Yati conducted all the simulations. Yati and AM analyzed the results and prepared the draft.

Acknowledgments

The authors gratefully acknowledge the Indian Institute of Technology Gandhinagar, India, for providing research facilities and financial support. We thank PARAM Ananta for computational resources.

Funding

There are no funding for this study.

Conflicts of Interest

The authors declare no conflicts of interest.

Data Availability Statement

The data that support the findings of this study are available from the corresponding authors upon reasonable request.

References

1. T. Chen, Y. Jin, H. Lv, et al., "Applications of Lithium-Ion Batteries in Grid-Scale Energy Storage Systems," *Transactions of Tianjin University* 26 (2020): 208–217.

2. S. Chu, Y. Cui, and N. Liu, "The Path towards Sustainable Energy," *Nature Materials* 16 (2017): 16–22.

3. Y. Yamada, J. Wang, S. Ko, E. Watanabe, and A. Yamada, "Advances and Issues in Developing Salt-Concentrated Battery Electrolytes," *Nature Energy* 4 (2019): 269–280.

4. M. J. Hossain, Q. Wu, E. J. Marin Bernardez, et al., "The Relationship between Ionic Conductivity and Solvation Structures of Localized High-Concentration Fluorinated Electrolytes for Lithium-Ion Batteries," *The Journal of Physical Chemistry Letters* 14 (2023): 7718–7731.

5. Y. Yamada and A. Yamada, "Review—Superconcentrated Electrolytes for Lithium Batteries," *Journal of the Electrochemical Society* 162 (2015): A2406.

6. K. Xu, "Nonaqueous Liquid Electrolytes for Lithium-Based Rechargeable Batteries," *Chemical Reviews* 104 (2004): 4303–4418.

7. G. Zhu, K. Wen, W. Lv, et al., "Materials Insights into Low-Temperature Performances of Lithiumion Batteries," *Journal of Power Sources* 300 (2015): 29–40.

8. K. Xu and C. A. Angell, "Sulfone-Based Electrolytes for Lithium-Ion Batteries," *Journal of the Electrochemical Society* 149 (2002): A920.

9. X. Sun and C. A. Angell, "Doped Sulfone Electrolytes for High Voltage Li-Ion Cell Applications," *Electrochemistry Communications* 11 (2009): 1418–1421.

10. L. Xue, K. Ueno, S.-Y. Lee, and C. A. Angell, "Enhanced Performance of Sulfone-Based Electrolytes at Lithium Ion Battery Electrodes, including the $LiNi_{0.5}Mn_{1.5}O_4$ High Voltage Cathode," *Journal of Power Sources* 262 (2014): 123–128.

11. Y. Ugata, Y. Chen, S. Sasagawa, et al., "Eutectic Electrolytes Composed of $LiN(SO_2F)_2$ and Sulfones for Li-Ion Batteries," *The Journal of Physical Chemistry C* 126 (2022): 10024–10034.

12. S. Mukherji, D. Brahma, and S. Balasubramanian, "Modeling High Concentration Bisaltin- Sulfolane Electrolytes and the Observation of Ligand-Bridged Cation-Pair Complexes," *The Journal of Physical Chemistry B* 128 (2024): 10675–10687.

13. S. Mukherji, N. V. Avula, and S. Balasubramanian, "Refined Force Field for Liquid Sulfolane with Particular Emphasis to Its Transport Characteristics," *ACS Omega* 5 (2020): 28285–28295.

14. K. Dokko, D. Watanabe, Y. Ugata, et al., "Direct Evidence for Li Ion Hopping Conduction in Highly Concentrated Sulfolane-Based Liquid Electrolytes," *The Journal of Physical Chemistry B* 122 (2018): 10736–10745.

15. A. Nakanishi, K. Ueno, D. Watanabe, et al., "Sulfolane-Based Highly Concentrated Electrolytes of Lithium Bis (trifluoromethanesulfonyl) Amide: Ionic Transport, Li-Ion Coordination, and Li–S Battery Performance," *The Journal of Physical Chemistry C* 123 (2019): 14229–14238.

16. M. Yati and A, "Microscopic Solvation Dynamics and Transport in LiFSA-Sulfone Electrolytes via Optimized Force Fields: A Classical MD Perspective," *The Journal of Physical Chemistry B* 129 (2025): 6919–6932.

17. Q. Yang, X. Lv, Y. Fu, K. Xu, and W. Guo, "Ligand Exchange of Li-Ion Solvation Sheath Enables Balanced Electrolytes," *Joule* 9 (2025): 101821.

18. X. Ren, S. Chen, H. Lee, et al., "Others Localized High-Concentration Sulfone Electrolytes for High-Efficiency Lithium-Metal Batteries," *Chem* 4 (2018): 1877–1892.

19. A. Abouimrane, I. Belharouak, and K. Amine, "Sulfone-Based Electrolytes for Highvoltage Li-Ion Batteries," *Electrochemistry Communications* 11 (2009): 1073–1076.

20. H. Jia, Y. Xu, L. Zou, et al., "Sulfone-Based Electrolytes for High Energy Density Lithium-Ion Batteries," *Journal of Power Sources* 527 (2022): 231171.

21. U. Tilstam, "Sulfolane: A Versatile Dipolar Aprotic Solvent," *Organic Process Research & Development* 16 (2012): 1273–1278,

22. M. Okoshi, C.-P. Chou, and H. Nakai, "Theoretical Analysis of Carrier Ion Diffusion in Superconcentrated Electrolyte Solutions for Sodium-Ion Batteries," *The Journal of Physical Chemistry B* 122 (2018): 2600–2609.

23. J. Self, K. D. Fong, and K. A. Persson, "Transport in Superconcentrated $LiPF_6$ and $LiBF_4$/Propylene Carbonate Electrolytes," *ACS Energy Letters* 4 (2019): 2843–2849.

24. K. R. Ramya, P. Kumar, A. Kumar, and A. Venkatnathan, "Interplay of Phase Separation, Tail Aggregation, and Micelle Formation in the Nanostructured Organization of Hydrated Imidazolium Ionic Liquid," *The Journal of Physical Chemistry B* 118 (2014): 8839–8847.

25. A. P. Sunda, V. M. Dhavale, S. Kurungot, and A. Venkatnathan, "Structure and Dynamics of Benzyl-NX_3 (X = Me, Et) Trifluoromethanesulfonate Ionic Liquids," *The Journal of Physical Chemistry B* 118 (2014): 1831–1838.

26. N. Singh, M. K. Jha, H. S. Dhattarwal, and H. K. Kashyap, "How NaFTA Salt Affects the Structural Landscape and Transport Properties of Pyrr1,3FTA Ionic Liquid," *The Journal of Chemical Physics* 158 (2023): 104502.

27. A. Malik and H. K. Kashyap, "Origin of Structural and Dynamic Heterogeneity in Thymol and Coumarin-Based Hydrophobic Deep Eutectic Solvents as Revealed by Molecular Dynamics," *Physical Chemistry Chemical Physics* 25 (2023): 19693–19705.

28. E. Crabb, A. Aggarwal, R. Stephens, Y. Shao-Horn, G. Leverick, and J. C. Grossman, "Electrolyte Dependence of Li^+ Transport Mechanisms in Small Molecule Solvents from Classical Molecular Dynamics," *The Journal of Physical Chemistry B* 128 (2024): 3427–3441.

29. S. Ikeda, S. Tsuzuki, T. Sudoh, et al., "Lithium-Ion Dynamics in Sulfolane-Based Highly Concentrated Electrolytes," *The Journal of Physical Chemistry C* 127 (2023): 13837–13845.

30. G. Kumar, T. R. Kartha, and B. S. Mallik, "Novelty of Lithium Salt Solution in Sulfone and Dimethyl Carbonate-Based Electrolytes for Lithium-Ion Batteries: A Classical Molecular Dynamics Simulation Study of Optimal Ion Diffusion," *The Journal of Physical Chemistry C* 122 (2018): 26315–26325.

31. M. J. Boyer, L. Vilčiauskas, and G. S. Hwang, "Novelty of Lithium Salt Solution in Sulfone and Dimethyl Carbonate-Based Electrolytes for Lithium-Ion Batteries: A Classical Molecular Dynamics Simulation

Study of Optimal Ion Diffusion," *Physical Chemistry Chemical Physics* 18 (2016): 27868–27876.

32. W. L. Jorgensen and J. Tirado-Rives, "The OPLS [optimized Potentials for Liquid Simulations] Potential Functions for Proteins, Energy Minimizations for Crystals of Cyclic Peptides and Crambin," *Journal of the American Chemical Society* 110 (1988): 1657–1666.

33. W. L. Jorgensen, D. S. Maxwell, and J. Tirado-Rives, "Development and Testing of the OPLS All-Atom Force Field on Conformational Energetics and Properties of Organic Liquids," *Journal of the American Chemical Society* 118 (1996): 11225–11236.

34. Yati, Y. Kokane, and A. Mondal, "Active-Learning Assisted General Framework for Efficient Parameterization of Force-Fields," *Journal of Chemical Theory and Computation* 21 (2025): 2638–2654.

35. S. Pronk, S. Páll, R. Schulz, et al., "GROMACS 4.5: A Highthroughput and Highly Parallel Open Source Molecular Simulation Toolkit," *Bioinformatics* 29 (2013): 845–854.

36. B. Hess, C. Kutzner, D. van der Spoel, and E. Lindahl, "GROMACS 4: Algorithms for Highly Efficient, Load-Balanced, and Scalable Molecular Simulation," *Journal of Chemical Theory and Computation* 4 (2008): 435–447.

37. M. J. Frisch, G. W. Trucks, H. B. Schlegel, et al., *Gaussian 09 Revision E.01* (Gaussian Inc, 2009).

38. L. Martínez, R. Andrade, E. G. Birgin, and J. M. Martínez, "PACKMOL: A Package for Building Initial Configurations for Molecular Dynamics Simulations," *Journal of Computational Chemistry* 30 (2009): 2157–2164.

39. T. Darden, D. York, and L. Pedersen, "Particle Mesh Ewald: An N Log (N) Method for Ewald Sums in Large Systems," *The Journal of Chemical Physics* 98 (1993): 10089–10092.

40. G. Bussi, D. Donadio, and M. Parrinello, "Canonical Sampling through Velocity Rescaling," *The Journal of Chemical Physics* 126 (2007): 014101.

41. H. J. Berendsen, J. v Postma, W. F. Van Gunsteren, A. DiNola, and J. R. Haak, "Molecular Dynamics with Coupling to an External Bath," *The Journal of Chemical Physics* 81 (1984): 3684–3690.

42. L. Van Hove, "Correlations in Space and Time and Born Approximation Scattering in Systems of Interacting Particles," *The Physical Review* 95 (1954): 249–262.

43. S. Mitra and R. Biswas, "Exploring the Capabilities and Limitations of the Van Hove Function to Understand Directional Correlations in Ion Movements Within Li-Ion Battery Electrolytes," *The Journal of Chemical Physics* 161 (2024): 064501.

44. J. Li, R. He, H. Yuan, F. Fang, G. Zhou, and Z. Yang, "Molecular Insights into the Effect of Asymmetric Anions on Lithium Coordination and Transport Properties in Salt-Doped Poly(ionic liquid) Electrolytes," *Macromolecules* 55 (2022): 6703–6715.

45. A. Ahmad, R. Köster, S. Kloth, and M. Vogel, "Comparative Molecular Dynamics Simulation Studies of Simple and Polymerized Ionic Liquids," *Soft Matter* 21 (2025): 5231–5241.

46. S. Mukherji, N. V. Avula, R. Kumar, and S. Balasubramanian, "Hopping in High Concentration Electrolytes-Long Time Bulk and Single-Particle Signatures, Free Energy Barriers, and Structural Insights," *The Journal of Physical Chemistry Letters* 11 (2020): 9613–9620.

47. M. Bonomi, D. Branduardi, G. Bussi, et al., "PLUMED: A Portable Plugin for Free-Energy Calculations with Molecular Dynamics," *Computer Physics Communications* 180 (2009): 1961–1972.

Supporting Information

Additional supporting information can be found online in the Supporting Information section.